



Validation of the multiaxial racetrack amplitude filter



Hao Wu^a, Marco Antonio Meggiolaro^{b,*}, Jaime Tupiassú Pinho de Castro^b

^a School of Aerospace Engineering and Applied Mechanics, Tongji University, Siping Road 1239, 200092 Shanghai, PR China

^b Pontifical Catholic University of Rio de Janeiro, PUC-Rio, Rua Marquês de São Vicente 225, Rio de Janeiro, RJ 22451-900, Brazil

ARTICLE INFO

Article history:

Received 7 October 2015

Received in revised form 23 December 2015

Accepted 15 January 2016

Available online 22 January 2016

Keywords:

Racetrack filter

Amplitude filter

Multiaxial fatigue

Non-proportional loading

Variable amplitude loading

ABSTRACT

Amplitude filters are a most important tool in practical fatigue analyses to manage their computational cost when, as usual, the measured load history is noisy, oversampled, too long, and/or contains too many non-damaging low-amplitude cycles or events. To reduce the calculation burden, such filters should not only eliminate noise and remove redundant oversampled data from the measured signal, but also neglect small amplitudes that do not cause fatigue damage. The veteran racetrack filter can perform all such tasks efficiently, however it is limited to uniaxial load histories. Multiaxial filtering techniques have been proposed in the past, however they fail to identify the most damaging events in several non-proportional histories, in addition to losing information on the load path shape. In this work, a new, fast, and efficient multiaxial version of the traditional racetrack filter is proposed to solve these issues, synchronously filtering complex loading histories while preserving all their significant reversals and equivalent ranges, and their load path shape as well, a most important feature for multiaxial fatigue analyses. Six and three-dimensional versions of the filter are proposed, respectively for invariant-based and critical-plane damage calculation approaches. The method allows not only the proper filtering of stress/strain histories at a given material point, but also of any history of multi-dimensional quantities such as forces, moments, and/or displacements acting at different points of a structure. The filter efficiency is evaluated from tension–torsion experiments in 316L stainless steel tubular specimens with challenging non-proportional path shapes.

© 2016 Elsevier Ltd. All rights reserved.

1. Introduction

Most service strain or load histories measured in practice have non-damaging low-amplitude events and non-negligible noise levels that introduce many irrelevant peak and valley events in the signal, which should not be considered in fatigue analyses. In fact, under real field conditions, these irrelevant events can be several orders of magnitude more frequent than the actual damaging events contained in the measured signal, a major practical problem when such signals must be used for structural integrity evaluations.

Frequency filters that can remove high-frequency noise are not appropriate for fatigue calculations, because they distort the signal and usually change the values of the load peaks and valleys, which are the main responsible for fatigue damage in rate-independent problems, where viscous effects can be ignored in the material behavior. Therefore, instead of frequency filters, *amplitude* filters are required instead in these cases to remove noise while

preserving the values and the order of the significant peaks and valleys of the strain or load history, regardless of time or frequency associated with them.

Load input filters have been proposed in the past to eliminate some of such undesirable events, since they much increase the numeric burden in fatigue analyses. In fact, they may even eventually render such analyses impracticable. However, so far there is no filtering procedure that can be considered a really appropriate tool to solve such important problems in practical fatigue damage calculations under multiaxial variable amplitude loading (VAL) conditions. This paper aims to help solving this situation, generalizing the racetrack idea that has been successfully used to solve uniaxial problems since the 1970's [1].

Uniaxial amplitude filters can be directly implemented in the cycle counting algorithm, usually based on the rainflow method [2–4]. The implementation of such an amplitude filter is rather simple if applied to the output of the cycle counting method, since it only requires the elimination of the counted amplitudes below a certain non-damaging threshold level, with or without considering mean/maximum stress effects.

However, the main advantage of such amplitude filters is to significantly decrease computational time, removing from the load

* Corresponding author.

E-mail addresses: wuhao@tongji.edu.cn (H. Wu), meggi@puc-rio.br (M.A. Meggiolaro), jtcastro@puc-rio.br (J.T.P. de Castro).

history noise and redundant data, as well as irrelevant non-damaging events, *before* counting them. In other words, they can only be useful in practice if the filtering process is efficiently performed *before* analyzing the fatigue damage caused by the load history. This is especially true for multiaxial VAL fatigue calculations based on the critical plane approach [5], which need rainflow counts of every projected history from every candidate plane. From the computational point of view such critical plane routines are intrinsically expensive, but nevertheless they are needed when modeling multiaxial fatigue damage in materials that tend to initiate a single dominant crack at critical points, like most metallic alloys.

In addition, the original rainflow procedure can only be started after the entire load history is known, increasing even more the computational cost as well as computer memory requirements, which can be quite significant for very long histories. Computational cost can be dramatically reduced with “real-time” rainflow algorithms, such as the pioneer Martin–Topper–Sinclair’s 1971 method [6], which essentially reproduces in real time the uniaxial rainflow algorithm as the load events are provided or measured. Several other “real-time” rainflow implementations have been proposed [7–11], which in essence are very similar to the original one [12]. In all of them, an amplitude filter could be easily included in the output step of the algorithm; but to decrease computational cost when dealing with real signals, in practice this filter should be applied *before* counting cycles, as discussed above.

The racetrack filter, originally proposed in [1] for uniaxial histories, can do that. It aims to eliminate from VAL histories small amplitude load events that do not induce fatigue damage, before applying any cycle counting method. In this way, the resulting condensed histories can accelerate both experiments and computations, focusing only on the few significant events that cause most or all of the damage. This filter has been successfully applied for managing practical uniaxial load histories, especially those measured by strain gages in actual field conditions, and is a well-proven tool capable of removing noise and most non-damaging events from real signals. Notice that this filter is only based on the signal amplitude, without including mean/maximum stress effects. Therefore, it is common practice in histories with tensile mean stresses to choose filter amplitudes significantly lower than the fatigue limit under zero stress ratio ($R = 0$).

However, the original racetrack filter unfortunately cannot be used in multiaxial fatigue calculations, even though amplitude filters are much more needed in such cases to decrease their intrinsically high computational cost. In fact, to properly measure load signals, it is necessary to oversample the digitalized data at a rate high enough not to distort the signal (theoretically, at least at a sampling frequency twice as high as the highest significant spectral component of the signal, but usually at a much higher rate in practice) [13]. Moreover, signals measured under real field conditions are always contaminated by noise, which introduce hopefully small but usually many irrelevant peaks and valleys that can make fatigue analyses impractical if not properly removed beforehand. Hence, the usual case in practical applications is to deal with oversampled data and noisy measurements.

A simplistic approach to decrease the number of points in oversampled multiaxial data would be to apply a peak/valley filter to each and every component of the loading, to remove all data points that are not peaks or valleys of any of their stress or strain components. But this filtering practice *cannot* be safely used in non-proportional (NP) multiaxial histories, for two reasons: first, the path between two load reversals is needed to evaluate the path-equivalent stress or strain ranges associated with each rainflow count, e.g. using a convex enclosure method or the Moment of Inertia (MOI) method [14]. Equivalent stress or strain ranges end up underestimated if too many points in the load path are filtered

out. Thus, some points along the path should not be eliminated from the load history, even if they do not constitute a load component reversal.

The second reason against using a simplistic non-reversal filter is because the reversal points obtained from a multiaxial rainflow algorithm do not necessarily occur at the reversal of one of the stress or strain components. For example, the relative von Mises strain, used in the Wang–Brown [15] and Modified Wang–Brown (MWB) [16] rainflow counts, may reach a peak value at a point that is neither a maximum nor a minimum of any strain component. But such most important points would be filtered out by a non-reversal filtering algorithm, resulting in non-conservative fatigue damage and life predictions.

One example of this simplistic filtering approach for multiaxial histories is the “Peaks Procedure” from [17], which filters out all events whose components are not peaks or valleys, potentially eliminating important load points that could have the highest von Mises stresses or strains in the load history, even though each individual component was not maximized. In addition, this procedure would store each and every event that constitutes a peak or valley from any single component, which for noisy measurements could result in no events at all being filtered out, even if the unavoidable noise had very low amplitudes.

An appropriate multiaxial amplitude filter should thus consider not only peaks and valleys, but also how a measured multiaxial loading path deviates from its course, evaluated by some metric such as the von Mises stress or strain. This fundamental feature is needed to avoid filtering out important counting points from multiaxial rainflow algorithms or significant paths that could affect the calculation of an equivalent stress or strain range, since all stress or strain components contribute altogether for the reversals that can be eliminated. Finally, once the original VAL history is condensed into a smoother history by discarding small amplitude ranges that cause negligible fatigue damage [18], as well as the unavoidable noise e.g. from actual strain measurements, the calculation effort can be much decreased without compromising its accuracy. Such filters are an almost indispensable tool for practical fatigue analyses.

In the next section, the uniaxial racetrack algorithm is reviewed, along with a physical peg-slot analogy that will be useful for the multiaxial generalization proposed in this work.

2. Uniaxial racetrack filter

Fig. 1 illustrates the uniaxial racetrack filter [1,19], condensing the original history from Fig. 1(a) into the history in Fig. 1(d), eliminating amplitudes smaller than a user-specified value r . Originally inspired by slalom ski races, this amplitude filter idea is to draw a *racetrack* of width $2r$ bounded by upper and lower *fences* that have the same profile as the original history, see Fig. 1(b). Every time a *driver* racing in this racetrack needs to change its direction a reversal point is identified, as seen in Fig. 1(c) where the driver needs to change twice its direction near points B and E, but not in points C and D (which are filtered out), because there is no need to avoid the fences associated with them.

Narrow tracks almost keep all the original reversals, while wider ones filter out most of the original loading history. As exemplified in Fig. 1, the condensed (by the racetrack amplitude filter) history does not change the order of the load events, an essential feature to account for plasticity memory effects.

Besides the driver (or perhaps slalom skier) analogy, the racetrack problem can also be regarded as a problem involving a small round peg P oscillating inside the slotted hole of a bar whose center is the point O, see Fig. 2, with total range $2r$. Initially, the peg and slot centers are aligned with point A, see Fig. 2(a). In the figures,

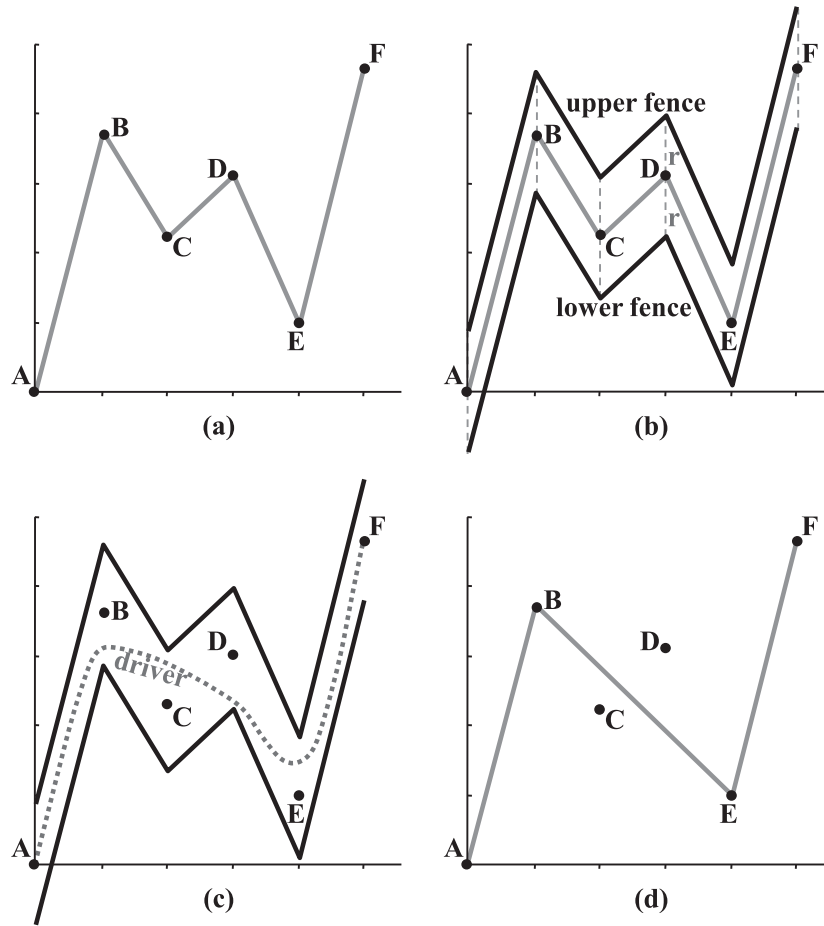


Fig. 1. Example of a uniaxial racetrack, showing: (a) the original history; (b) the racetrack defined between the upper and lower fences; (c) the driver path from A to F; and (d) the filtered history.

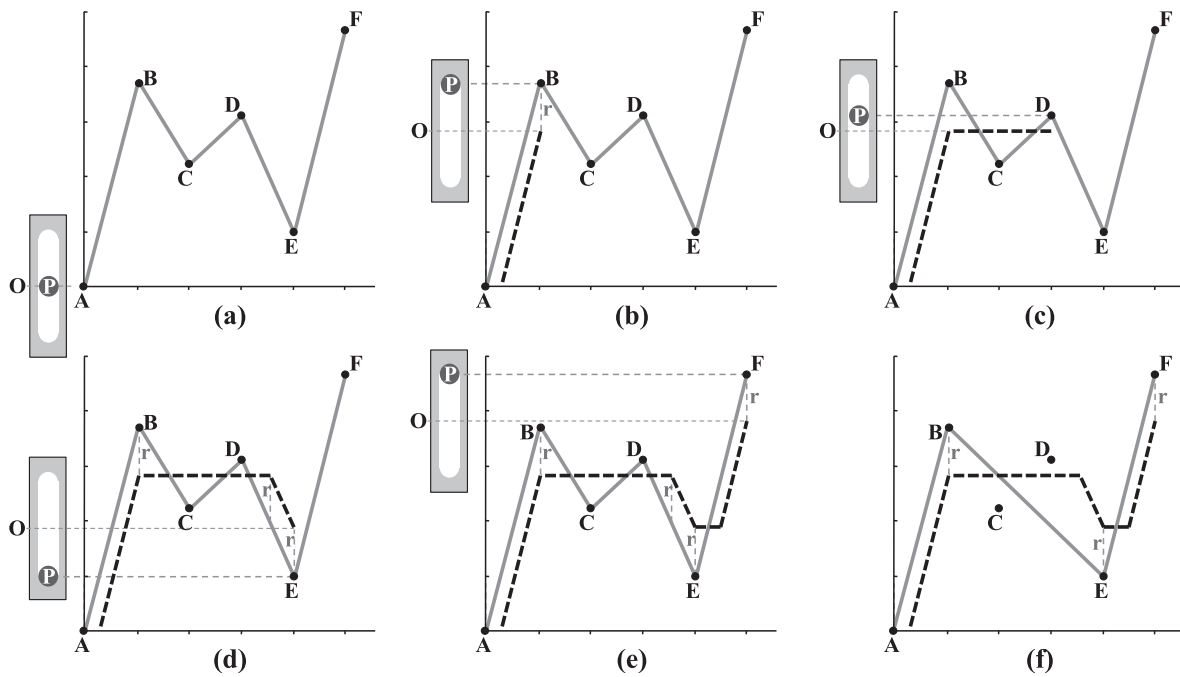


Fig. 2. The uniaxial racetrack filter is analogous to a peg oscillating while it follows the original history inside a bar with a slotted hole with center O and slot length $2r$.

the dark dashed line represents the path of point O, while the filtered history only accounts for peg translations that effectively dragged the slotted bar.

The peg initially moves up along the path AB, until reaching the upper limit of the slotted bar, forcing the bar to move up until reaching point B, see Fig. 2(b). The path BCD does not involve any translation of the slotted bar, thus points C and D will be filtered out, see Fig. 2(c). Then, both paths DE and EF involve slotted bar translations, see Fig. 2(d) and (e). After the initial point A, only the peg locations P at the end of a translation of the slotted bar are stored in the filtered history ABEF, see Fig. 2(f). This nice way of looking at the racetrack filter can be generalized for the multi-axial case as follows.

3. The Multi-axial Racetrack Filter (MRF)

Based on the uniaxial peg-slot analogy from the previous section, a multi-axial generalization of the racetrack algorithm has been introduced in [18] and is expanded and detailed here. This Multi-axial Racetrack Filter (MRF) is based on a representation of the stress or strain history in a six-dimensional (6D) space, along with a user-defined filtering amplitude r (similar to the one required for the 1D case). However, the proposed multi-axial racetrack algorithm is not limited to filter amplitudes in stress or strain histories at a single material point. It can also be applied to histories containing any multi-dimensional physical quantities whose norm needs to be filtered out using a user-specified amplitude r , even if it includes data measured at different locations, as explained later in Section 7.

For the time being, assume that a small peg \vec{P} is allowed to move in this 6D stress or strain space. However, instead of being restricted within a 1D slot, it is kept inside a 6D hypersphere of center \vec{O} and radius r . When the peg reaches the hypersphere surface and tries to move out of it, both the peg and the hypersphere translate altogether, similarly to the 1D slotted bar example. To illustrate this idea, Fig. 3 shows a 2D tension–torsion example of a hypersphere (reduced to a circle in this simple case) translation caused by the peg movement from its current position \vec{P}_i to the next \vec{P}_{i+1} , where \vec{n}_i is the current normal vector that defines the surface translation direction (still to be determined), and b_i , a_i , and d_i are distances (measured in stress or strain units) used in the amplitude filtering algorithm.

Using the next peg location \vec{P}_{i+1} from the load history, combined with the current location \vec{O}_i of the hypersphere center, and a known translation direction \vec{n}_i , the values of the dimensions b_i , a_i , and d_i can be calculated from

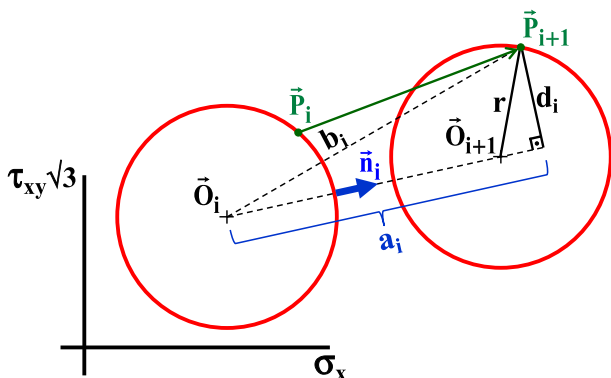


Fig. 3. Hypersphere translation along \vec{n}_i , caused by a peg movement from \vec{P}_i to \vec{P}_{i+1} . For this 2D tension–torsion example, the hypersphere simply becomes a circle.

$$b_i^2 = (\vec{P}_{i+1} - \vec{O}_i)^T \cdot (\vec{P}_{i+1} - \vec{O}_i), a_i = (\vec{P}_{i+1} - \vec{O}_i)^T \cdot \vec{n}_i, \quad \text{and} \\ d_i^2 = b_i^2 - a_i^2 \quad (1)$$

where the distance b_i must be greater than the radius r to guarantee that the next loading event \vec{P}_{i+1} is outside the current hypersphere, otherwise there is no surface translation.

While $a_i \geq 0$ and $d_i \leq r$, the next peg location \vec{P}_{i+1} can still be located on the border of the hypersphere translated in the \vec{n}_i direction, for a translation of the center to (see Fig. 3):

$$\vec{O}_{i+1} = \vec{O}_i + \left(a_i - \sqrt{r^2 - d_i^2} \right) \cdot \vec{n}_i \quad (2)$$

The algorithm continues for the next \vec{P}_{i+2} , and so on. Fig. 4 shows two consecutive translations where the conditions $a_i \geq 0$ and $d_i \leq r$ are satisfied, allowing the hypersphere translation direction to remain constant, i.e. $\vec{n}_i \equiv \vec{n}_{i-1}$. In this example, point \vec{P}_i can be filtered out, since it does not alter the translation direction during the (multi-axial) load history path $\vec{P}_{i-1} \vec{P}_i \vec{P}_{i+1}$. This filtering process that happens while the hypersphere is translated is called here *dynamic filtering*.

In the multi-axial racetrack algorithm, the first loading point from the load history, located in the general case in the 6D stress or strain space, defines the initial locations \vec{P}_1 of the peg and \vec{O}_1 of the hypersphere center, see Fig. 5. No hypersphere translation happens while the peg moves inside it, therefore in this example points \vec{P}_2 through \vec{P}_{i-1} are filtered out, in a process called here *static filtering* (because it does not involve hypersphere translations), see Fig. 5(a).

The translation direction \vec{n}_i must be defined when the peg reaches for the first time the hypersphere border and tries to move outside it. One of the simplest proposed translation direction rules assumes the normal vector \vec{n}_i is determined from the segment that joins the current hypersphere center \vec{O}_i and the next peg location \vec{P}_{i+1} , i.e.

$$\vec{n}_i = (\vec{P}_{i+1} - \vec{O}_i) / b_i \quad (3)$$

as seen in Fig. 5(a).

This simple rule has two advantages: (i) it is easy to calculate, without requiring information about future points \vec{P}_{i+2} , \vec{P}_{i+3} , etc.; and (ii) the value of \vec{n}_i does not have to be recalculated at every load step, as in other improved rules for the translation direction of the hypersphere center, discussed later on.

The only points (besides the initial \vec{P}_1) that are not filtered out are the ones where some significant path kinking happens due to $d_i > r$, and the ones where a load “reversal” forces a change of more than 90° in the hypersphere translation direction, i.e. $\vec{n}_{i-1} \cdot \vec{n}_i < 0$ and therefore $a_i < 0$. In these kinking or reversal cases, the new hypersphere translation direction could be determined by the proposed rule $\vec{n}_i = (\vec{P}_{i+1} - \vec{O}_i) / b_i$. The kinking and reversal criteria could happen at the same time, see Fig. 5(b), where the path kinks at \vec{P}_i because \vec{P}_{i+1} has $d_i > r$ (kinking criterion) as well as $\vec{n}_{i-1} \cdot \vec{n}_i < 0$, and thus $a_i < 0$ (reversal criterion). The hypersphere center translation during a kinking and/or reversal of the load path can be simply calculated by

$$\vec{O}_{i+1} = \vec{O}_i + (b_i - r) \cdot \vec{n}_i \quad (4)$$

because the distance between \vec{O}_i and \vec{P}_{i+1} is equal to b_i , see Fig. 3.

The initial point and all kinking and/or reversal points then constitute the filtered history. The reversal criterion $a_i < 0$ keeps track of abrupt changes in loading direction that might characterize a “peak” condition, while the kinking criterion $d_i > r$ guarantees that

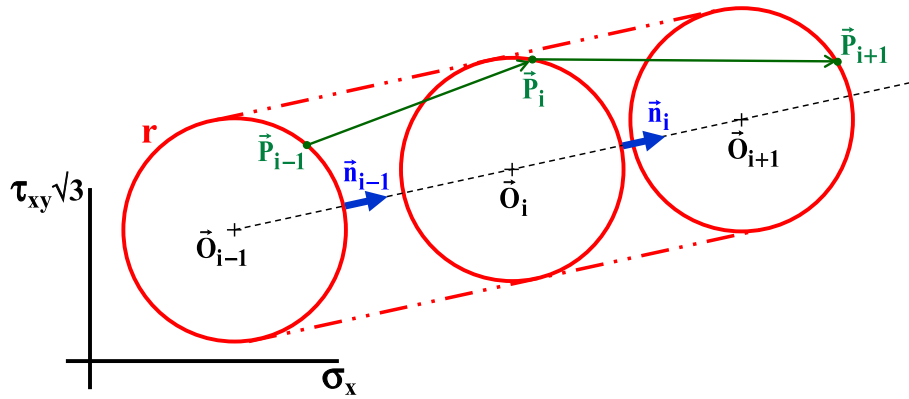


Fig. 4. Circle (or hypersphere) translations along $\bar{n}_i \equiv \bar{n}_{i-1}$, caused by the path $\tilde{P}_{i-1}\tilde{P}_i\tilde{P}_{i+1}$. Note that *dynamic filtering* eliminates the point \tilde{P}_i from the load history because it does not alter the hypersphere translation direction.

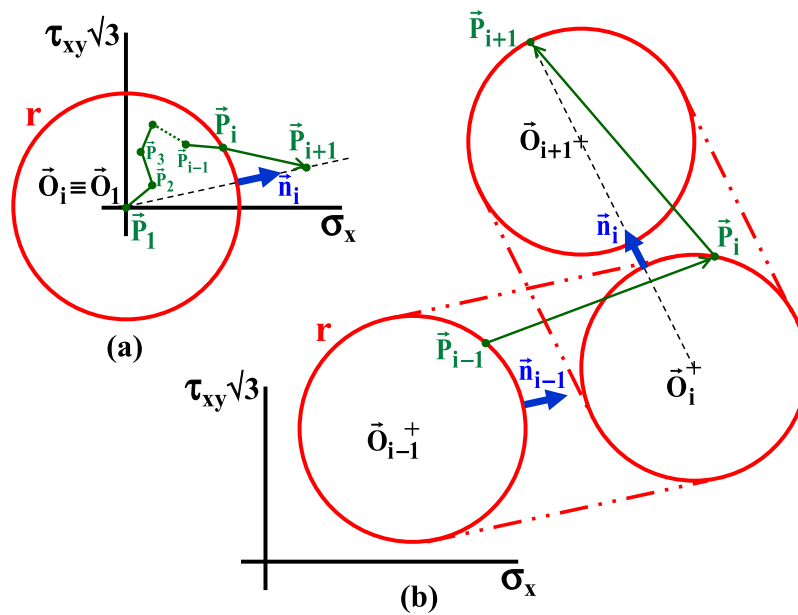


Fig. 5. Hypersphere location (a) during its first translation and (b) during a kinking of the load path.

a significant curvature of the load path history between two points is accounted for without assuming it is a straight line. Path curvature is important in the calculation of path-equivalent stress and strain ranges [14], because the use of a straight path could lead to a non-conservative range calculation when compared to the actual NP curved stress or strain path. Fig. 6 shows a flowchart with all the procedures involved in the proposed MRF algorithm, using the simple translation rule from Eq. (3). Note that it exactly reproduces the classic uniaxial racetrack algorithm if \vec{P} and \vec{O} are represented by scalars.

4. MRF tension–torsion example

Fig. 7(a) shows an example of a normal \times effective shear stress path obtained under tension–torsion, which can be used to exemplify the step-by-step application of the MRF algorithm. Fig. 7(b) shows the filtered history for a given relatively large filter amplitude r , where only four out of the sixteen original data points were not filtered, significantly decreasing the computational cost of multiaxial fatigue life calculations for this load history. In this figure, the points that suffered static filtering are marked with an

\times , while the dynamically-filtered ones are represented with triangular markers.

Notice once again the immense practical importance of these MRF *amplitude* filtering procedures. Indeed, since the calculation of multiaxial fatigue damage accumulation is an intrinsically intensive computational procedure, it is most important to eliminate from the calculation effort all points that are not essential for its result, i.e. all points that do not cause significant fatigue damage.

Fig. 7(c) compares the (dashed) original history with the filtered one. The filtered data tends to the original one as the filter amplitude r decreases, at the cost of increasing the number of unfiltered points, see Fig. 7(d) and (e). In practice, a relatively large r value can be initially chosen, and then decreased until the calculated damage converges.

Fig. 7(f) shows outputs from the simplistic “Peaks Procedure” proposed in [17], where only points that constitute the reversal of at least one component are kept. The output from the original history in (a) has very few filtered events, showing that the “Peaks Procedure” is very inefficient when applied to noisy signals. On the other hand, if applied to the already denoised path $\tilde{P}_1\tilde{P}_5\tilde{P}_{10}\tilde{P}_{16}$ from (b), the stress state \tilde{P}_1 is inappropriately filtered out, since it is not

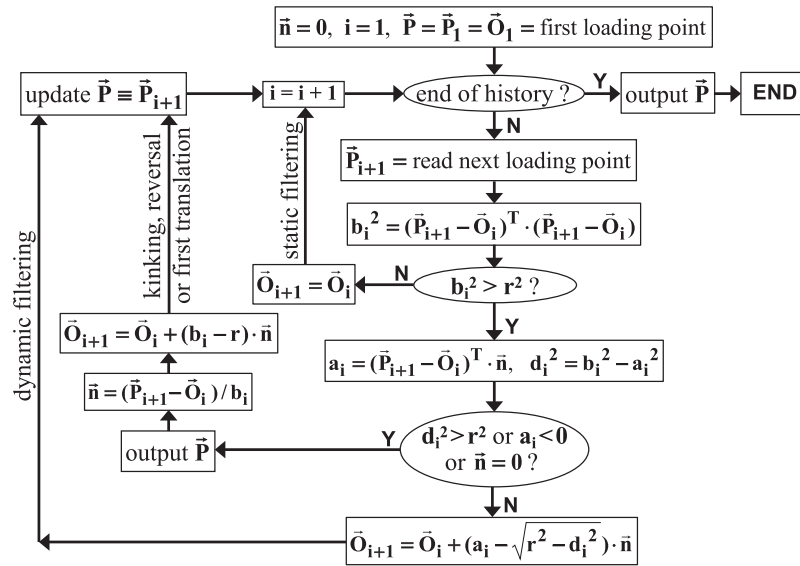


Fig. 6. Proposed MRF algorithm, with static and dynamically-filtered history resulting from the \bar{P} output values, where \bar{n} is the hypersphere translation direction.

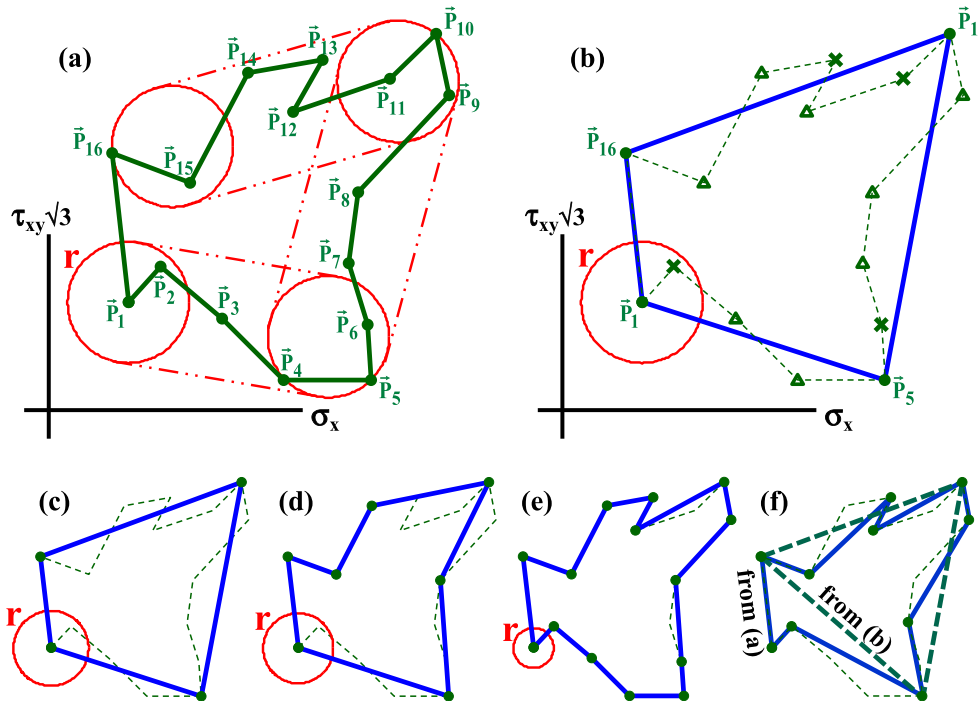


Fig. 7. Multi-axial racetrack filter applied to a tension–torsion history path with 16 points, showing (a) the translating hyperspheres, (b) the static and dynamically-filtered points (respectively marked as \times and triangles), and the effect of decreasing the filter amplitude r , resulting in histories with (c) four, (d) seven, and (e) fourteen points; and (f) the outputs using the simplistic “Peaks Procedure” proposed in [17] from the unfiltered (a) and filtered (b) histories.

a reversal from any applied load component, even though it defines with point \bar{P}_{10} the highest von Mises range from the history (thus probably the most damaging event). Such a “Peaks Procedure” triangular output $\bar{P}_5\bar{P}_{10}\bar{P}_{16}$ also shown in Fig. 7(f) would probably lead to non-conservative damage calculations not only for von Mises invariant-based damage models, but also for models based on the critical plane approach, since such an important state \bar{P}_1 would not be kept to consider its projected effect on each candidate plane. In summary, the “Peaks Procedure” is not efficient for noisy signals and potentially non-conservative for denoised data.

5. Optimized translation direction for the MRF

The hypersphere translation direction $\bar{n}_i = (\bar{P}_{i+1} - \bar{O}_i)/b_i$ from Eq. (3) is an arbitrary value that only takes into account a direction trend of the next stress or strain point \bar{P}_{i+1} . An optimized normal unit direction \bar{n}_i to maximize the filter efficiency would be a function of not only the point \bar{P}_{i+1} , but also of all further points $(\bar{P}_{i+2}, \bar{P}_{i+3}, \dots)$ until the next kinking/reversal along the load path.

This issue becomes evident in Fig. 8(a), which shows a hypersphere translation based solely on the direction of \bar{P}_{i+1} , a non-

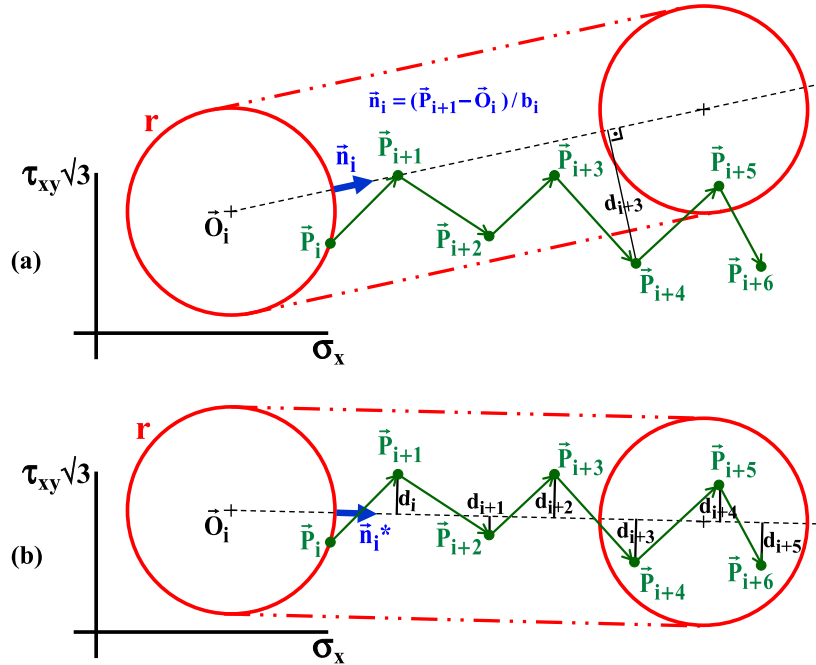


Fig. 8. Dynamic filtering process for hypersphere translations in (a) non-optimized $\bar{n}_i = (\bar{P}_{i+1} - \bar{O}_i)/b_i$ and (b) optimized \bar{n}_i^* directions.

optimized choice that would force in this example a kink at \bar{P}_{i+3} , because \bar{P}_{i+4} ends up outside the translating hypersphere due to its distance $d_{i+3} > r$ calculated for the \bar{n}_i direction. Fig. 8(b) shows the same example for a translation in an optimized unit direction \bar{n}_i^* , which better reflects the direction trend of points \bar{P}_{i+1} through \bar{P}_{i+6} , allowing all of them to be filtered out without kinking or reversals because all d_i through d_{i+5} (calculated for the \bar{n}_i^* direction instead of \bar{n}_i) are within the filter amplitude r . Such optimized direction results in a more efficiently filtered history, i.e. with fewer remaining points for the same filter amplitude r .

It is important to note that such \bar{n}_i^* must be recalculated every time a new point is introduced. So, the initial value of \bar{n}_i^* would only be based on \bar{P}_{i+1} , and thus become equal to $\bar{n}_i = (\bar{P}_{i+1} - \bar{O}_i)/b_i$. But as the next \bar{P}_{i+2} is introduced, the optimized \bar{n}_i^* direction is updated based on both \bar{P}_{i+1} and \bar{P}_{i+2} . After introducing \bar{P}_{i+3} , \bar{n}_i^* is updated based on \bar{P}_{i+1} , \bar{P}_{i+2} and \bar{P}_{i+3} , and so on.

So, the optimized translation direction \bar{n}_i^* in Fig. 8(b) has been calculated after the introduction of \bar{P}_{i+6} , based on all points \bar{P}_{i+1} through \bar{P}_{i+6} . This \bar{n}_i^* is such that the maximum distance to the translation line among $d_i, d_{i+1}, \dots, d_{i+5}$ is minimized, as seen in the figure. In this way, the optimal direction \bar{n}_i^* (which changes at every new loading input) prevents any of such distances from becoming larger than the filter amplitude r , where a kinking would need to occur from the condition $d_i > r$.

The optimization becomes a linear programming problem that tries to find a straight line that minimizes the maximum distance to the loading history points, known as the *minimax regression problem*. The straight line associated with the resulting optimized translation direction \bar{n}_i^* is the *first order Chebyshev approximation* of the further loading path points before the next load path kinking/reversal (\bar{P}_{i+1} through \bar{P}_{i+6} in the example) that goes through the current hypersphere center (\bar{O}_i), which can be found using the *Remez exchange algorithm* [20] detailed in [21]. The optimized version of the proposed MRF can then be implemented from the Fig. 6 flowchart by replacing the unit normal direction \bar{n}_i with

the optimized \bar{n}_i^* , which however must be recalculated every time a new point is introduced in the filtering process.

For a given \bar{O}_i , the successive optimized directions \bar{n}_i^* (calculated after every new load point input) indeed maximize the number of filtered points along the hypersphere translation, while respecting the filter amplitude r . Notice however that the resulting output is not necessarily a global optimum regarding filter efficiency, because other optimized directions might lead to different \bar{O}_i locations, which by chance could end up resulting in a larger number of filtered points in the subsequent steps. Nevertheless, an eventual global optimization of the filter would probably require knowledge of the entire load history beforehand, while involving computationally-intensive iterative searches for the filter output with least number of points. Such a globally-optimized MRF would probably result in only a small improvement of filter efficiency over the \bar{n}_i^* approach, but with a much higher computational cost, not required or practical for most engineering applications.

6. Stress and strain spaces and sub-spaces for the MRF

The proposed MRF can be applied to any stress or strain space, for instance $[\sigma_x \ \sigma_y \ \sigma_z \ \tau_{xy} \ \tau_{xz} \ \tau_{yz}]^T$ or $[\varepsilon_x \ \varepsilon_y \ \varepsilon_z \ \gamma_{xy} \ \gamma_{xz} \ \gamma_{yz}]^T$ for a general 6D history. To better correlate the relative importance between normal and shear components, another proposal could include effective shear stresses and strains, correlated by von Mises' $\sqrt{3}$ factor: $[\sigma_x \ \sigma_y \ \sigma_z \ \tau_{xy}\sqrt{3} \ \tau_{xz}\sqrt{3} \ \tau_{yz}\sqrt{3}]^T$ or $[\varepsilon_x \ \varepsilon_y \ \varepsilon_z \ \gamma_{xy}/\sqrt{3} \ \gamma_{xz}/\sqrt{3} \ \gamma_{yz}/\sqrt{3}]^T$. In this way, the filter amplitude r could better consider normal and shear components for equivalent von Mises stresses and strains (assuming plastic strains dominate over elastic ones for the strain space case, to avoid having to deal with the elastic component of the Poisson ratio).

However, the above 6D spaces mix deviatoric and hydrostatic components, not providing a clear physical meaning of the filter amplitude r . Alternatively, a given stress history could be

represented in a 6D stress space composed of a 5D deviatoric space \vec{s} [22]

$$\vec{s} \equiv [\sigma_x - (\sigma_y + \sigma_z)/2 \quad (\sigma_y - \sigma_z)\sqrt{3}/2 \quad \tau_{xy}\sqrt{3} \quad \tau_{xz}\sqrt{3} \quad \tau_{yz}\sqrt{3}]^T \quad (5)$$

with the sixth dimension equal to the hydrostatic stress component σ_h multiplied by a scaling constant α_h .

It is not difficult to prove that the norm of \vec{s} is equal to the von Mises stress σ_{Mises} , therefore all distances and filter amplitudes in this 5D sub-space have a physical meaning: they are the relative von Mises stresses [15], which would be equal to the von Mises stress range $\Delta\sigma_{Mises}$ for a straight path between two stress states. In this way, for a constant σ_h , the filter amplitude r would incorporate a physical meaning, becoming a threshold $\Delta\sigma_{Mises}$ below which the stress history is filtered out. For a variable σ_h , the filter amplitude would relate with the metric $\sqrt{\Delta\sigma_{Mises}^2 + (\alpha_h \cdot \Delta\sigma_h)^2}$ from this proposed 6D space.

Furthermore, if the scaling constant α_h is calibrated e.g. proportionally to the fitting constants from Sines' [23] or Crossland's [24] stress-based damage models, then the distances in the 6D space $\{\vec{s}, \alpha_h \cdot \sigma_h\}$ could be roughly (but not exactly) proportional to the respective damage parameters $\Delta\tau_{Mises} + \alpha_s \cdot \sigma_{hmean}$ or $\Delta\tau_{Mises} + \alpha_c \cdot \sigma_{hmax}$, respectively, where $\Delta\sigma_{Mises} = \Delta\tau_{Mises}\sqrt{3}$. In this way, the filter amplitude r would incorporate another physical meaning, becoming a threshold damage parameter below which the stress history is filtered out.

Analogously, a given strain history could be represented in the 6D space $\{\vec{\epsilon}, \alpha_h \cdot \epsilon_h\}$, where ϵ_h is the hydrostatic strain and $\vec{\epsilon}$ is the 5D deviatoric strain vector

$$\vec{\epsilon} \equiv [\epsilon_x - (\epsilon_y + \epsilon_z)/2 \quad (\epsilon_y - \epsilon_z)\sqrt{3}/2 \quad \gamma_{xy}\sqrt{3}/2 \quad \gamma_{xz}\sqrt{3}/2 \quad \gamma_{yz}\sqrt{3}/2]^T \quad (6)$$

where α_h would need to be calibrated from the adopted strain or energy-based damage model.

Note however that, according to the critical plane approach [5], it is the normal stress σ_\perp perpendicular to the critical plane that affects the damage induced by $\Delta\tau$ (or by any other parameter assumed as the cyclic damage driving force in the multiaxial fatigue damage model), not the hydrostatic component σ_h . Since σ_\perp is not an invariant, a multiaxial filter including σ_\perp in its stress space would need to be evaluated for every candidate plane. Nevertheless, the above 6D spaces could still be used in the critical plane approach, as long as the chosen filter amplitude r is significantly smaller than a threshold value associated with the fatigue limit from any candidate plane, to avoid non-conservative results from the elimination of damaging events.

Alternatively, the proposed MRF could be applied at each and every candidate plane projection, to filter out non-damaging events from each plane, using e.g. the 3D spaces

$$[\tau_A \quad \tau_B \quad \sigma_\perp]^T \quad \text{or} \quad [\gamma_A \quad \gamma_B \quad \epsilon_\perp]^T \quad (7)$$

where the subscripts A and B represent both in-plane and out-of-plane shear directions of a candidate plane, and \perp stands for its normal direction.

Clearly, every candidate plane (at the critical point of the analyzed component) would involve a different MRF process and thus different filtered loading points. These 3D spaces would be able to filter out small non-damaging shear events (through the first two components from each 3D space) and small non-damaging tensile events (through the last one), becoming applicable to shear-based damage models (such as Fatemi–Socie's [25]), tensile-based damage models (e.g. the multiaxial generalization of Smith–Watson–Topper's [26]), and even multiaxial models that combine shear

and normal damage [27–29]. Independently of the adopted 6D or 3D space, the MRF algorithm from Fig. 6 remains unchanged, confirming the generality of the proposed filtering method.

7. Generalization of the MRF to any physical space

The proposed MRF algorithm is not limited to stress or strain histories at a single material point. It can also be applied to a history of any multi-dimensional physical quantity that must be synchronously filtered according to its norm with an amplitude r , even if it includes data measured at different locations. Such a generalized MRF version can have several practical engineering applications, as discussed next.

For instance, consider a complex load history induced by M imposed forces, moments, and/or displacements $F_1(t), F_2(t), \dots, F_M(t)$ applied at various points of a structure, as schematized in Fig. 9. If such a complex loading history is measured during a time interval $0 \leq t \leq T$ using M force/torque/displacement sensors at a high sampling rate, as usually needed to not distort the measured signals, then a very large number N of sampled data points would be captured and stored in a huge $N \times M$ matrix. Moreover, in practical applications the measured signals will always be contaminated by unavoidable noise, which much increase the number of irrelevant peak and valleys in the data files, and thus the computational effort needed to analyze them if not properly filtered.

Indeed, just imagine that this sampled data will be used e.g. in computationally-intensive Finite Element (FE) calculations. It is highly desirable to reduce the $N \times M$ input data matrix to a much lower and manageable $N' \times M$ size, see Fig. 9, as long as no significant information is lost, meaning no potentially damaging event is neglected. But it certainly does not make sense to apply a uniaxial racetrack filter to each column of the data matrix, because the resulting filtered history would lose synchronicity, since each column in general would filter out points from different instants and lead to load columns with different number of points.

Instead, all force/moment/displacement inputs need to be filtered altogether, a task that could be performed using the proposed MRF algorithm adopting an M -dimensional space $[\alpha_1 \cdot F_1(t) \quad \alpha_2 \cdot F_2(t) \quad \dots \quad \alpha_M \cdot F_M(t)]^T$, where $\alpha_1, \alpha_2, \dots, \alpha_M$ are weights that describe the relative importance among the M load history components. This approach allows as well the mixing of different physical quantities with different units into the same space. The same algorithm from Fig. 6 can be adopted to solve this demanding filter problem, however considering M -dimensional (instead of 6D) quantities and hyperspheres.

For instance, if for $M=3$ inputs a force $F_1(t)=1000$ N is assumed to have a roughly similar effect on a structure as a moment $F_2(t)=100$ Nm or a displacement $F_3(t)=0.01$ m applied at different locations, then a 3D space $[\alpha_1 \cdot F_1(t) \quad \alpha_2 \cdot F_2(t) \quad \alpha_3 \cdot F_3(t)]^T$ could be used in the MRF algorithm with e.g. $\alpha_1=1$,

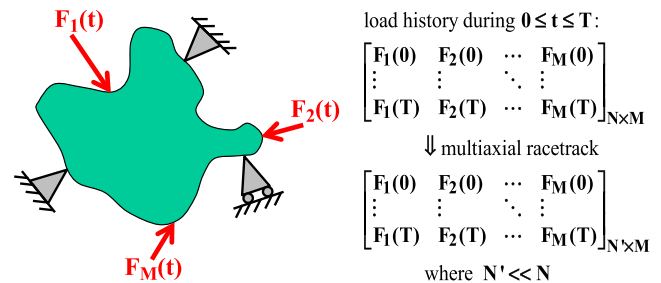


Fig. 9. The MRF could be applied to a history of M imposed forces, moments, and/or displacements $F_1(t), F_2(t), \dots, F_M(t)$ acting at various points of a structure, decreasing the number of samples N to a much lower N' without losing any significant information.

$\alpha_2 = 1000/100 = 10$, and $\alpha_3 = 1000/0.01 = 100,000$. Moreover, if e.g. force variations $|\Delta F_1| < 50$ N can be neglected, then the algorithm could use the same filter amplitude $r = \alpha_1 \cdot |\Delta F_1| = 50$ to filter out all three load history quantities, since the load component weights α_i would take care of their relative importance, as well as of unit conversions.

The calibration of the weight factors α_i could be performed from the linear elastic (LE) influence factors k_i of each input force/moment/displacement $F_i(t)$ with respect to a chosen material point. In such a calibration, a single LE FE calculation on the entire structure or component is performed for a static unit value $F_i = 1$ of each applied loading F_i . The LE influence factors that correlate each unit load and the resulting stresses are then evaluated in each direction at a chosen material point, usually a candidate critical point such as a notch tip. Clearly, these influence factors k_i are not dimensionless and in fact may have different dimensions, because they correlate local stresses or strains with e.g. forces, moments, or displacements. The weight factors α_i can then be calibrated from a normalization based e.g. on the first value k_1 , namely $\alpha_i = k_i/k_1$, for every $i = 1, \dots, M$.

As expected, every candidate critical point (or any other point of interest) would have a different set of influence and weight factors, since a given input $F_i(t)$ could affect much more some points of the structural component than others. To minimize computational cost, a single representative set of weight factors could be chosen for the entire component, allowing the MRF to be evaluated only once, instead of once for every point of interest. Such a single set could be calibrated from each largest (or perhaps average) influence factor k_i among all points of interest of the structure. This single set approach should provide a good cost-benefit for the subsequent calculations, as long as the filter amplitude r is small enough to avoid filtering out significant events from any of the points of interest.

The value of the MRF amplitude r can also be iteratively increased by the user until the number of rows N' in the filtered history is low enough to be used with some desired reduced computational cost e.g. in a FE program.

Similarly, as very high filter amplitudes r lose information on significant events of the original history (filtering out too many data points), successive lower r -values could then be chosen to assure convergence of the desired damage parameter.

8. Mean/maximum stress effects in the MRF

Mean/maximum stress effects can also be included in the MRF algorithm, adopting a filter amplitude r that depends on the current stress level. In this way, a small stress or strain amplitude event could be filtered out if associated with a (non-damaging) low-stress level, while another event with the same amplitude could be preserved if happening under a (more damaging) high-stress level. The variable value of r must be calculated in real time, thus it cannot depend on peak or mean stresses along a load event, because it would require cycle identification and information about future events. Instead, mean/maximum stress effects are modeled in the MRF in a simplified way, as a function of the current (instantaneous) hydrostatic σ_h or normal σ_\perp stress along the load path, respectively for invariant-based [23,24] and critical-plane models [25–29], where σ_\perp is the projected normal stress perpendicular to the considered candidate plane.

For instance, for Crossland's invariant-based model [24], the stress history could be represented in the 5D deviatoric stress space \vec{s} (instead of the 6D space $\{\vec{s}, \alpha_h \cdot \sigma_h\}$), while adopting a σ_h -dependent variable filter amplitude

$$r = \Delta\sigma_{Mises}/2 = \Delta\tau_{Mises}\sqrt{3}/2 = (\beta_c\sqrt{3}) - (3\sqrt{3}\alpha_c) \cdot \sigma_h \quad (8)$$

where β_c and α_c are Crossland's material constants.

On the other hand, for e.g. Fatemi–Socie's critical-plane model [25], the projected shear strain history on the considered candidate plane could be represented in the 2D strain space $[\gamma_A \ \gamma_B]^T$, while adopting a σ_\perp -dependent variable filter amplitude

$$r = r_0/(1 + \alpha_{FS} \cdot \sigma_\perp/S_{Yc}) \quad (9)$$

where r_0 is a user-defined filter level based on a shear strain amplitude, S_{Yc} is the cyclic yield strength, and α_{FS} is Fatemi–Socie's adjustable parameter.

In this way, the filter amplitude r becomes instantaneously smaller for higher σ_h or σ_\perp stress levels, to avoid filtering out damaging events. Similar expressions for such a variable r can be derived for other damage models.

9. Experimental results

To verify the efficiency of the proposed MRF procedures, tension–torsion experiments are performed on annealed tubular 316L stainless steel specimens in a multiaxial servo-hydraulic testing machine, shown in Fig. 10. Since some experiments in this work involve large compression strains, the minimum wall thickness of the specimen is chosen as 2.0 mm to avoid local buckling. On the critical section, the tubular specimen has external and internal diameters $d_{ext} = 16$ mm and $d_{int} = 12$ mm.

Engineering stresses and strains are calculated from load and torque measurements made by the machine load cells and from a commercial axial/torsional extensometer, and then converted to true stresses and strains. The engineering shear stresses include the elastoplastic gradient correction recommended by ASTM E2207-08 [30], which is especially important in this relatively thick-walled tubular specimen to deal with stress gradient effects across its thickness. The cyclic properties of this 316L steel are obtained from uniaxial tests, resulting in fitted Ramberg–Osgood uniaxial cyclic hardening coefficient $H_c = 874$ MPa and exponent $h_c = 0.123$, with Young's modulus $E = 193$ GPa, Poisson ratio $\nu = 0.3$, and $G = E/(2 + 2\nu) \cong 74$ GPa.

The analyzed experiments consist of strain-controlled tension–torsion load cycles applied to the tubular specimens, for a very challenging NP strain paths proposed in [31], named here “Maltese Cross” for their particular shape, see Fig. 11. As seen in this figure, for a given normal strain amplitude ε_a , each period of the applied normal-effective shear strain path $\varepsilon_x \times \gamma_{xy}/\sqrt{3}$ follows the sequence OABHAOCBDCOEDFEOGHFGO. Several load periods were then applied to the same specimen successively for each of the

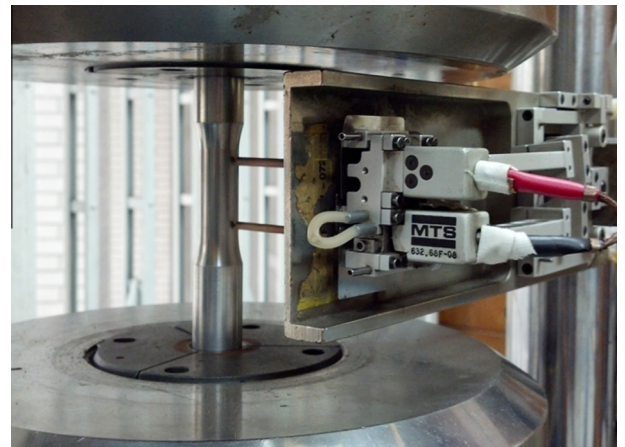


Fig. 10. Tension–torsion testing machine and extensometer mounted on a tubular specimen.

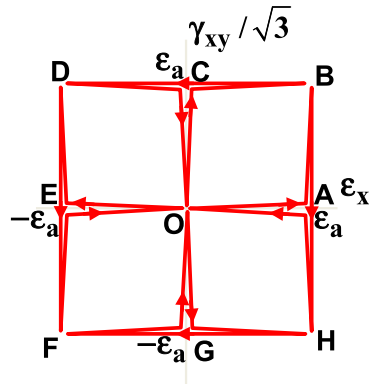


Fig. 11. Applied $\varepsilon_x \times \gamma_{xy}/\sqrt{3}$ strain paths on the same tension–torsion tubular specimen, with successively applied amplitudes $\varepsilon_a = 0.2\%$, 0.4% , 0.6% and 0.7% .

chosen strain amplitudes $\varepsilon_a = 0.2\%$, 0.4% , 0.6% and 0.7% . The resulting normal-effective shear stress path $\sigma_x \times \tau_{xy}/\sqrt{3}$ is particularly challenging, because it involves high NP hardening effects and transients [22], as well as several reversal points (according to the MWB multiaxial rainflow [16] or to critical-plane rainflow methods [32]) that are not reversals of any stress component, see Fig. 12.

Fig. 12 shows 119,939 experimentally measured data points, as well as the MRF output (using the simpler non-optimized version of the algorithm) for a chosen filter amplitude $r = 7$ MPa. Notice in the figure how the 37,496 remaining points after the MRF can almost exactly describe the original history, capturing not only all reversal points but also the path shape, which is a most important feature for equivalent range calculations.

Fig. 13 shows the outputs from the proposed filter and from the “Peaks Procedure” for the last loading period from Fig. 12. The “Peaks Procedure” significantly alters the shape of the loading path due to the absence in the algorithm of a user-defined filter amplitude, potentially resulting in non-conservative predictions from adopting lower path-equivalent ranges. The “Peaks Procedure”

was not worse in this case only because the “Maltese Cross” path has very sharp and well-defined reversals, which become as well the reversals of von Mises equivalent histories and of projected components on candidate planes. For a more general loading history this is not as usual, as discussed before for Fig. 7, where \bar{P}_1 defined the highest von Mises range from the denoised path $\bar{P}_1\bar{P}_5\bar{P}_{10}\bar{P}_{16}$, despite not being a reversal from any applied stress component.

Another alternative approach besides the “Peaks Procedure” is the multidimensional wavelet transformation [33], which has several applications in signal and image denoising. Despite powerful, this approach is more computationally-intensive than geometrically-based algorithms such as the MRF, and most importantly it usually acts to eliminate high-frequency signals. If such high-frequency events are actual disturbances and not sensor noise, then they should not be eliminated, because they could significantly influence the location of load peaks/reversals/kinks and associated path-equivalent ranges, thus affecting the predicted fatigue life. In other words, the smoothening effect of any frequency filter tends to lose information on the signal peaks, useful to eliminate spikes in some applications, but inappropriate for fatigue calculations since it can eliminate important peaks and corners in the load path. Instead, filters purely based on amplitude should be used in fatigue, such as the MRF, at least for rate-independent problems.

It is important to note that the MRF is only able to exactly detect all load path corners if sufficiently small filter amplitudes are chosen. Otherwise, the MRF might perform a shortcut on that corner, however always within the chosen filter amplitude. As discussed above, such corners are important due to the non-linear relation between load ranges and fatigue damage, therefore they should be preserved in the best possible way.

To evaluate the performance of the proposed MRF, filter amplitudes $r = 1, 2, 3, \dots, 15$ MPa were successively applied to the stress path from Fig. 12. Fig. 14 shows the number of remaining points after the MRF for each chosen r . As expected, higher values of r filter out more loading events, resulting in fewer remaining points.

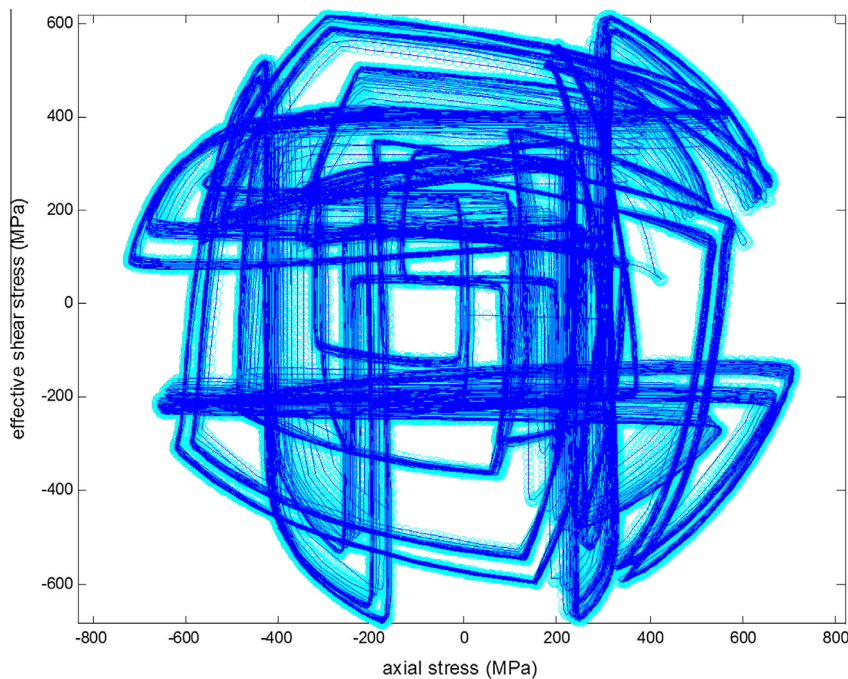


Fig. 12. Resulting $\sigma_x \times \tau_{xy}/\sqrt{3}$ stress paths drawn from 119,939 experimentally measured data points (light circular markers, from strain amplitudes 0.2% , 0.4% , 0.6% and 0.7% successively applied to the same tubular tension–torsion specimen), showing a very good agreement in both ranges and shape with the MRF output with only 37,496 points (dark lines), for a filter amplitude $r = 7$ MPa.

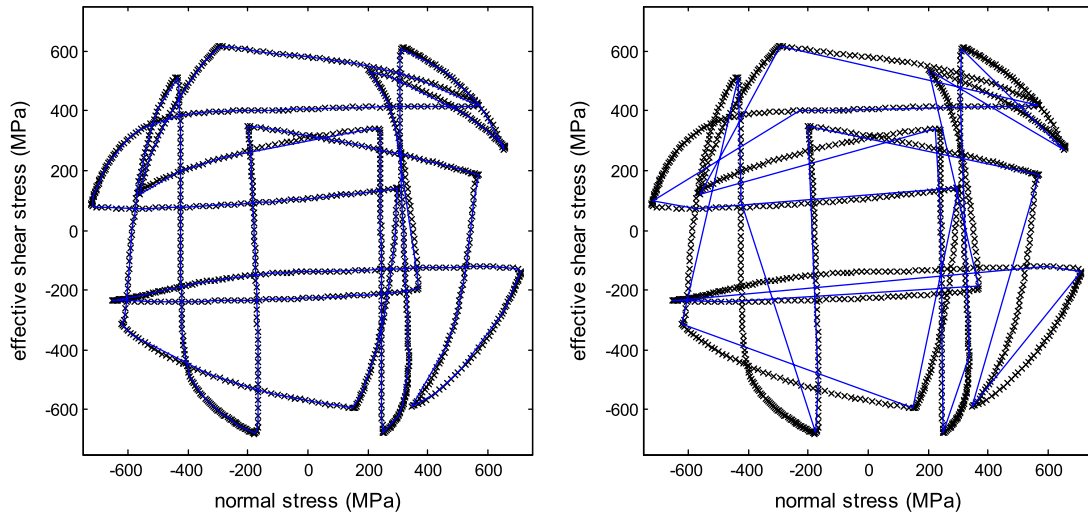


Fig. 13. Measured (x markers) and filtered (solid lines) $\sigma_x \times \tau_{xy}\sqrt{3}$ stress paths for the last period from Fig. 12, either using the MRF for a filter amplitude $r = 7$ MPa (left), or using the “Peaks Procedure” proposed in [17] (right).

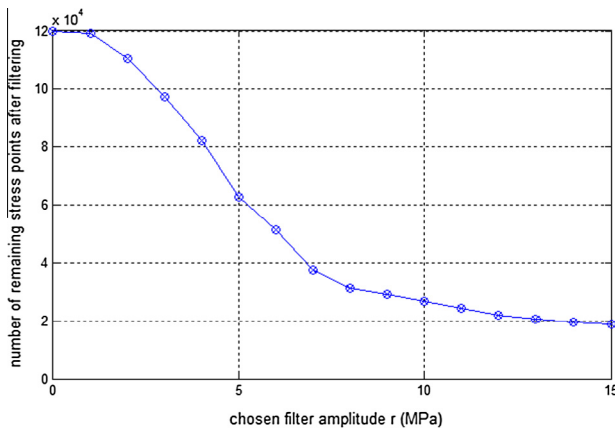


Fig. 14. Number of remaining points after applying the MRF to the stress history from Fig. 12, as a function of the chosen filter amplitude r (in MPa).

For this loading history, Fig. 14 suggests that filter amplitudes r near 7 MPa might provide a good tradeoff between filtering efficiency (filtering out about 2/3 of the original data points, down from 119,939 to 37,496) and damage calculation accuracy (guaranteeing that no filtered stress range will be off from the original history more than 7 MPa).

Moreover, as seen in Fig. 13(left), for the 7 MPa filter amplitude all corner points from the original path were preserved by the MRF within 7 MPa, and the path shapes were almost exactly preserved, resulting in the same multiaxial rainflow count (within 7 MPa for each counted event) using the Modified Wang–Brown method [16]. Even after including path-equivalent range calculations in the damage model using surface enclosures [14], there was no significant difference in the resulting calculated damage, since the associated prismatic or elliptical enclosures are not sensitive at all to small changes in the path shape, as long as the path corners are well preserved.

Much lower filter amplitudes, such as $r = 2$ MPa, would not cause any noticeable improvement in the calculated damage (either from a MWB or a critical plane approach), however the number of remaining points would still be high, 110,454 in this case, much increasing computational cost. On the other hand, a much higher $r = 15$ MPa would be able to reduce the original sample down to 18,924 points, however with a few noticeable paths not very accurately reproduced by the filtered history.

In any case, for all filter amplitudes shown in Fig. 14, the proposed MRF was able to identify the equivalent range of the most damaging event (within the chosen filter amplitude), not missing the most important reversal points for either MWB or critical plane approaches. Such an exact match of the highest events is only not observed for very high (coarse) filter amplitudes. Moreover, for all remaining events, the MRF guaranteed that the filtered equivalent ranges were never off from the original history more than the value of the chosen filter amplitude r , as expected, even for high (coarse) values of r . Notice once again that these encouraging results were obtained using the non-optimized translation direction $\vec{n}_i = (\vec{P}_{i+1} - \vec{O}_i)/b_i$; in an implementation using the optimized translation direction \vec{n}_i^* , the MRF would be able to filter out even more points for each given r , but at a higher computational cost due to the need to apply the Remez exchange algorithm [20–21] for every input point.

Each application of the MRF to the 119,939 points from the measured history, in the non-optimized implementation, took only about 0.7 s to run in the Matlab® environment in an i7-4790 CPU at 3.6 GHz with 16 GB RAM memory, a small value compared to the time required for the associated damage computations, especially in the critical plane approach. Therefore, the proposed MRF algorithm is not only accurate, but also computationally efficient. For instance, the entire sensitivity analysis from Fig. 14 took only about 11 s to be calculated.

Notice however that the computer time for the MRF process could be much higher if memory allocation for the filter output is not performed in an efficient way within the programming environment, a purely computational issue, but one that certainly cannot be disregarded. For instance, an inefficient dynamic memory allocation of the 37,496 output points from the chosen amplitude $r = 7$ MPa could rise computer time from 0.7 s to 4.3 s, while for the 110,454 output points from $r = 2$ MPa it could rise from 0.7 s to 60.2 s.

Surely the “Peaks Procedure” is much faster (0.03 s instead of 0.7 s in the above example) since it only involves a single-pass search along all loading points. However this does not justify its use, since it can filter out highly-damaging loading states. The impact on the accuracy of the calculated damage depends on the adopted model. But its order of magnitude can be roughly estimated for a simple square-shaped tension–torsion history, slightly skewed such that the “Peaks Procedure” output is a triangle, as in Fig. 7(f), with about half the area of the original square. In at least

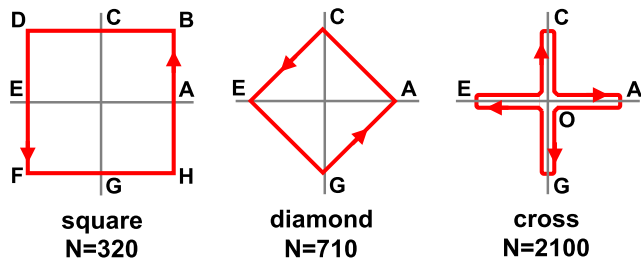


Fig. 15. Strain paths $\epsilon_x \times \gamma_{xy}/\sqrt{3}$ with equal normal and effective shear ranges 0.8%, which induce significantly different fatigue crack initiation lives (in number of blocks) in tubular 304 stainless steel specimens [35].

one of the candidate plane projections, the filtered normal or shear range could be about half the unfiltered one. For a high-cycle fatigue calculation assuming Wöhler's exponent 11 (a median value for steels [34]) and zero mean loads, the "Peaks Procedure" would underestimate by a factor of up to $2^{11} = 2048$ the damage of such a filtered range on certain candidate planes, potentially missing the critical one. Such an unacceptable error could be eliminated using the proposed MRF with an appropriate filter amplitude, certainly worth the slightly higher computational time (only $0.7 - 0.03 = 0.67$ s for the 119,939-point case).

Less dramatic but still significant non-conservative errors would arise from the "Peaks Procedure" in low-cycle fatigue, in which loading ranges and fatigue damage are associated with exponents much lower than 11, typically $-1/c = -1/(-0.59) \cong 1.7$ for steels [34], where c is Coffin–Manson's plastic exponent. This effect can be verified from Itoh's [35] tension–torsion experiments on three 304 stainless steel tubular specimens subjected to square, diamond and cross-shaped tension–torsion strain histories, all of them with normal strain ranges $\Delta\epsilon \cong 0.8\%$ equal to the effective shear strain ranges $\Delta\gamma/\sqrt{3} \cong 0.8\%$, see Fig. 15.

The square-shaped $A-B-C-D-E-F-G-H-A$ path resulted in an initiation life of $N = 320$ load blocks, while the diamond-shaped $A-C-E-G-A$ resulted in $N = 710$ and the cross-shaped $O-A-O-C-O-E-O-G-O$ in $N = 2100$ load blocks (which could also be interpreted as 4200 cycles, if the cross was decomposed into two perpendicular uniaxial paths, each with one cycle per period). If e.g. due to measurement noise in the square path the magnitudes of the strains at the centers A, C, E and G were slightly higher than at the corners B, D, F , and H , then the "Peaks Procedure" would filter out these corners (since they would not constitute reversals of any applied load component), resulting in the diamond path.

On the other hand, if in the cross path the unloading events did not exactly reach the origin O as suggested in the figure, then such unloadings would not constitute load reversals, and the "Peaks Procedure" would also result in the same diamond path $A-C-E-G-A$. Therefore, the square and cross-shaped paths can be seen as limit cases for the errors induced by the "Peaks Procedure" with respect to the diamond path, which would predict the same diamond-shaped filtered history and thus the same life in number of blocks. As a result, even if the adopted damage model was able to exactly predict the measured 710-block life of the diamond path, the application of the "Peaks Procedure" would underestimate the cross-path life by a factor of $2100/710 \cong 3$, and non-conservatively overestimate the square-path life by $(710 - 320)/320 \cong 122\%$.

10. Conclusions

In this work, a multiaxial version of the racetrack filter originally proposed in [18] was improved and optimized. It is applicable to general non-proportional multiaxial histories, being very fast and relatively simple to implement following the provided flowchart, while exactly reproducing the original

racetrack filter for uniaxial histories. The proposed filter treats all load events sequentially, therefore it preserves load order, an important issue to correctly predict load sequence effects. Six-dimensional stress and strain spaces have been proposed for damage models based on invariants such as von Mises and hydrostatic components. A 3D version of the filter has also been presented, applicable for the critical plane approach. The proposed method is very versatile, allowing the synchronous filtering of stress and strain histories acting at a given material point, or of any history of multi-dimensional quantities such as forces, moments, and/or displacements acting at different points of a structure, with several practical applications in engineering. The filter efficiency was evaluated from tension–torsion experiments following complex non-proportional histories, demonstrating its ability to quickly and significantly condense the input history without losing information on significant reversals, ranges or load path shapes.

Acknowledgements

This work was supported in part by the National Natural Science Foundation of P.R. China under Grant No. 11302150. CNPq-Brazil provided research fellowship for Prof. Marco A. Meggiolaro.

References

- [1] Fuchs HO, Nelson DV, Burke MA, Toomay TL. Shortcuts in cumulative damage analysis. SAE automobile engineering meeting paper 730565; 1973.
- [2] Matsuishi M, Endo T. Fatigue of metals subjected to varying stress. *Jpn Soc Mech Eng* 1968.
- [3] ASTM E 1049. Standard practices for cycle counting in fatigue analysis. ASTM International.
- [4] Downing SD, Socie DF. Simple rainflow counting algorithms. *Int J Fatigue* 1982;4(1):31–40.
- [5] Bannantine JA, Socie DF. A variable amplitude multiaxial fatigue life prediction method. *Fatigue under biaxial and multiaxial loading*, vol. 10. Springer; 1991. p. 35–51.
- [6] Martin JF, Topper TH, Sinclair GM. Computer based simulation of cyclic stress–strain behavior with applications to fatigue. *Mater Res Stand MTRSA* 1971;11(2):23–8.
- [7] Conle FA. A computer simulation assisted statistical approach to the problem of random fatigue. M.Sc. thesis. University of Waterloo; 1974.
- [8] Glinka G, Kam JCP. Rainflow counting algorithm for very long stress histories. *Int J Fatigue* 1987;9(4):223–8.
- [9] Bannantine JA, Comer JJ, Handrock JL. *Fundamentals of metal fatigue analysis*. Englewood Cliffs, NJ: Prentice-Hall; 1990.
- [10] Amzallag C, Gerey JP, Robert JL, Bahaud J. Standardization of the rainflow counting method for fatigue analysis. *Int J Fatigue* 1994;16:287–93.
- [11] Meggiolaro MA, Castro JTP. Automation of the fatigue design under variable amplitude loading using the ViDa software. *Int J Struct Integr* 2010;1:1–6.
- [12] McInnes CH, Meehan PA. Equivalence of four-point and three-point rainflow cycle counting algorithms. *Int J Fatigue* 2008;30(3):547–59.
- [13] Dally JW, Riley WF. *Experimental stress analysis*. 4th ed. College House; 2001.
- [14] Meggiolaro MA, Castro JTP. An improved multiaxial rainflow algorithm for non-proportional stress or strain histories – Part I: Enclosing surface methods. *Int J Fatigue* 2012;42:217–26.
- [15] Wang CH, Brown MW. Life prediction techniques for variable amplitude multiaxial fatigue – Part 1: Theories. *J Eng Mater Technol* 1996;118:367–70.
- [16] Meggiolaro MA, Castro JTP. An improved multiaxial rainflow algorithm for non-proportional stress or strain histories – Part II: The modified wang–brown method. *Int J Fatigue* 2012;42:194–206.
- [17] Bannantine JA. A variable amplitude multiaxial fatigue life prediction method. FCP report n.151, University of Illinois at Urbana-Champaign; 1989.
- [18] Meggiolaro MA, Castro JTP, Wu H. Shortcuts in multiple dimensions: the multiaxial racetrack filter. I workshop challenges in multiaxial fatigue, Urbino, Italy; 2015.
- [19] Nelson DV, Fuchs HO. Predictions of cumulative fatigue damage using condensed load histories. In: *Fatigue under complex loading*. SAE; 1977.
- [20] Remez EY. Sur la détermination des polynômes d'approximation de degré donnée. *Commun Kharkov Math Soc* 1934;10:41–63.
- [21] Luenberger DG. *Introduction to linear and nonlinear programming*. Addison-Wesley Publishing Company; 1973.
- [22] Meggiolaro MA, Castro JTP. Prediction of non-proportionality factors of multiaxial histories using the Moment Of Inertia method. *Int J Fatigue* 2014;61:151–9.
- [23] Sines G. Behavior of metals under complex static and alternating stresses. In: *Metal fatigue*. McGraw-Hill; 1959. p. 145–69.

- [24] Crossland B. Effect of large hydrostatic pressures on the torsional fatigue strength of an alloy steel. *International Conf on Fatigue of Metals*, London: IMechE; 1956. p. 138–49.
- [25] Fatemi A, Socie DF. A critical plane approach to multiaxial damage including out-of-phase loading. *Fatigue Fract Eng Mater Struct* 1988;11:149–66.
- [26] Smith RN, Watson P, Topper TH. A stress–strain parameter for the fatigue of metals. *J Mater* 1970;5(4):767–78.
- [27] Papuga J, Ruzicka M. Two new multiaxial criteria for high cycle fatigue computation. *Int J Fatigue* 2008;30:58–66.
- [28] Susmel L, Lazzarin P. A bi-parametric Wöhler curve for high cycle multiaxial fatigue assessment. *Fatigue Fract Eng Mater Struct* 2002;25:63–78.
- [29] Susmel L. Multiaxial fatigue limits and material sensitivity to non-zero mean stresses normal to the critical planes. *Fatigue Fract Eng Mater Struct* 2008;31:295–309.
- [30] ASTM E2207-08. Standard practice for strain-controlled axial-torsional fatigue testing with thin-walled tubular specimens; 2013.
- [31] Socie DF, Marquis GB. *Multiaxial fatigue*. Warrendale, PA: Society of Automotive Engineers, Inc.; 2000.
- [32] Langlais TE, Vogel JH, Chase TR. Multiaxial cycle counting for critical plane methods. *Int J Fatigue* 2003;25:641–7.
- [33] Young RK. *Wavelet theory and its applications*. Springer; 1993.
- [34] Meggiolaro MA, Castro JTP. Statistical evaluation of strain-life fatigue crack initiation predictions. *Int J Fatigue* 2004;26:463–76.
- [35] Itoh T, Sakane M, Ohnami M, Socie DF. Nonproportional low cycle fatigue criterion for type 304 stainless steel. *ASME J Eng Mater Technol* 1995;117:285–92.